

# An augmented Lagrangian algorithm for recovery of ice thickness in unidirectional flow using the Shallow Ice Approximation.

Elizabeth K. McGeorge<sup>a</sup>, Miguel Moyers-Gonzalez<sup>a,\*</sup>, Phillip L. Wilson<sup>a,b</sup>,  
Mathieu Sellier<sup>c</sup>

<sup>a</sup>*Te Kura Pāngarau — School of Mathematics and Statistics, Level 4, Jack Erskine Building,  
University of Canterbury, Private Bag 4800, Christchurch 8140, New Zealand*

<sup>b</sup>*Te Pūnaha Matatini Centre of Research Excellence, University of Auckland, Auckland, New  
Zealand*

<sup>c</sup>*Department of Mechanical Engineering, University of Canterbury, Christchurch, New  
Zealand*

---

## Abstract

A key parameter in ice flow modelling is basal slipping at the ice-bed interface as it can have a large effect on the resultant ice thickness. Unfortunately, its contribution to surface observations can be hard to distinguish from that of bed undulations. Therefore, inferring the ice thickness from surface measurements is an interesting and non-trivial inverse problem. This paper presents a method for recovering dually the ice thickness and the basal slip using only surface elevation and speed measurements. The unidirectional shallow ice approximation is first implemented to model steady state ice flow for given bedrock and basal slip profiles. This surface is then taken as synthetic observed data. An augmented Lagrangian algorithm is then used to find the diffusion coefficient which gives the best fit to observations. Combining this recovered diffusion with observed surface velocity, a simple Newton's method is used to recover both the ice thickness and basal slip. The method was successful in each test case and this implies that it should be possible to recover both of these parameters in two-dimensional cases also.

**Keywords:** Inverse problems, Augmented Lagrangian, Ice flows, Shallow ice

---

\*Corresponding author.

Email address: miguel.moyersgonzalez@canterbury.ac.nz (Miguel Moyers-Gonzalez)

## 1. Introduction

Ice thickness recovery from surface data is a popular problem among those working on land ice models, with many different sectors all seeking to understand the intricacies of the problem. Governments need the information for policy and natural resource planning. Geo-scientists need more detailed resolution in the bed topography to fully understand glacial processes [1]. Statisticians question how certain bed inversions can be given the uncertain nature of many factors in any model [2, 3], and mathematicians wonder if the solution is even unique.

As stated in the Summary for Policymakers chapter of the 2019 IPCC Special Report on the Ocean and Cryosphere in a Changing Climate [4], all people on earth depend directly or indirectly on the ocean and cryosphere. The cryosphere refers to the frozen component of the earth system and includes land ice in the form of snow, glaciers, ice caps, permafrost, and ice sheets, as well as frozen parts of the ocean such as those surrounding Antarctica and Greenland. It also includes frozen lakes and rivers [5]. Oceans cover 71% of the Earth surface and land ice covers approximately 10% of Earth's land area. Populations living in coastal environments and mountainous regions are particularly vulnerable to changes in ocean and cryosphere. Around 680 million people live in low lying coastal zones and another 670 in high mountain regions (totally approximate 20% of the 2010 global population). For these people, ocean and cryosphere provide life-sustaining services such as food and water supply, renewable energy, and benefits for health and well-being, cultural values, tourism, trade, and transport. Given the potentially large impact of climate projections on human livelihood, comprehensive and accurate predictive models for ocean and cryosphere dynamics are needed to support policy planning in governments.

A key component of cryosphere dynamics is that of land ice. The contribution of land ice to global mean sea level (GLMS) rise for medium emissions scenarios is projected to be at least 0.10 m by 2100 with some models predicting a

contribution of up to 0.27 m [6]. Church et al. [6] identified one of the main  
30 contributors to this rise as the melting of land ice. To track the evolution of ice  
mass, ice thickness measurements or estimations are needed. However, these  
are costly measurements to take over large areas. Due to this, scientists often  
estimate ice thickness based on a few measurements or from surface data. To  
make these estimations first requires some model of how the ice flows.

35 Ice sheets have two main characteristics; (1) they exhibit gravity-driven creep  
flow which is sustained by the underlying sloped geography and (2) their growth  
and/or decline is controlled by the accumulation and/or ablation due to snow fall  
and/or melting. Ice can be categorised as an incompressible, nonlinear, viscous,  
heat conducting fluid [7] and can be described mathematically by the full Navier-  
40 Stokes (NS) flow equations together with a Generalized Newtonian Constitutive  
Law (Glen's Law). Many methods of approximating the conservation equations  
for ice sheets have been proposed in the last century. These approximations  
are not all equal; each have their own advantages and drawbacks. Typically,  
the more simplistic a model, the faster and easier it is to use in computations.  
45 But, of course, these simple models can omit processes which are important for  
accurately capturing the flows' behaviour.

One of the most widely used approximations for ice sheet flow is the shallow-  
ice approximation (SIA) [8, 9]. The SIA simplifies the full Stokes equations  
by performing a scaling analysis to obtain simplified field equations for the ice  
50 sheet flow. This scaling assumes the ice extent is much larger than its thickness.  
Blatter et al. [10] advise caution when applying the SIA to processes on smaller  
scales where the assumptions may no longer be valid, for example, anisotropic  
basal sliding or locally steep basal topography. Simply put, in the SIA model,  
gravity-driven ice flow is solely balanced by basal drag neglecting longitudinal  
55 and transverse stresses, as well as vertical stress gradients [11]. Despite potential  
drawbacks, the SIA is used widely in ice flow modelling as it reduces a three  
dimensional flow with four unknown fields into problem into a two dimensional  
problem with a single unknown field. This makes it computationally simple in  
comparison to the full Stokes where a full force balance has to be calculated at

60 each step.

Due to the complexity of ice flow behaviour, recovering the ice thickness from only surface measurements is a non-trivial inverse problem. In current state of the art models, it has been shown that variations in recovered ice thickness can be as large as the ice thickness recovered. The recovered thickness is also very  
65 sensitive to input data [12]. These variations are due to, in part, placing excess assumption on the flow behaviour, such as the no-slip condition at the base [13, 14, 15, 16, 17].

Imposition of a no-slip condition simplifies the inverse problem, allowing much faster computation. However, basal slip is known influence the flow behaviour [18]  
70 and should be included if possible. Flow speed is modulated by the presence, or lack thereof, of friction at the ice-bedrock boundary [19] as well as the steepness of the underlying slope. Since the free surface of an ice flow is affected by both basal slip and bedrock topography, separating the effects of these two factors in the recovery is difficult [20, 21].

75 Bueler and Brown [22] use the shallow-shelf approximation (SSA) as a sliding law for the shallow-ice approximation. The SSA, derived originally by Morland [23] and Macayeal [24], assumes that basal shear stresses are negligible since the shelf is floating and so longitudinal stresses dominate. They hoped to bridge the gap between observations of varying velocity across ice sheets and modelled  
80 velocities. In their paper, they use an average of velocities from the shallow shelf approximation and the non-sliding shallow-ice approximation in the energy conservation and mass continuity equations. The resultant velocity field exhibits realistic behaviour as seen in observations of ice streams. One way to try to decouple the effects of bed topography and basal slip is to assume some a priori  
85 knowledge of the particular ice flow. Zorzut et al. [25] included basal slip in their ice thickness estimations for the Monte Tronador glaciers using the parallel flow approximation. The parallel flow approximation assumes that glaciers deform only by simple shear such that flow lines are parallel [19]. To do this, they assumed a linear proportionality between basal speed and surface speed and used  
90 measured points of ice thickness to compute an estimation of the factor. Recent

work towards understanding the coupled behaviour of bed topography and basal slip in the ice surface presentation is promising. Monnier and Boscs [21] take surface data together with an initial ice thickness estimate from measurements and then improve upon it. This is done by optimising an objective functional to  
95 match the SIA modelled surface and observations (sometimes called variational data assimilation or VDA). Adding to this, Monnier and Zhu [26] consider an alternative form of the SIA, which combines all unknown parameters in one variable. Incorporated in this variable is allowance for basal slipping, however it is not explicitly recovered.

100 Further work is also being done towards understanding the sensitivity of inversions to their inputs. Kyrke-Smith et al. [27] investigated whether there is any correlation between seismic observations of basal acoustic impedance and the basal slip obtained from surface-to-bed inversions. Using data from the Pine Island Glacier, they found that, on the kilometre scale, there was no significant  
105 correlation between acoustic impedance and basal slip. However, using averaged values along profiles on the glacier resulted in a stronger correlation causing them to hypothesise that there may be correlation over length scales which are important to overall ice sheet flow. This sort of research using available and easy to measure data helps to restrict uncertainty in the basal slip parameter.  
110 Kyrke-Smith et al. [28] further went on to consider the effect of bed resolution in basal slip inversions using the Pine Island data.

Bedrock data is costly and time consuming to acquire and is not available in many cases. It is therefore useful to analyse the effect of the bed on basal slip inversions. To do this, Kyrke-Smith et al. look at the sensitivity of inversion  
115 methods to the accuracy of the bedrock profile prescribed. In particular, they consider the separated effect of basal drag due to the bed topography (form drag) and the drag due to bed properties (skin drag). They showed that a significant amount of basal shear calculated in inversion may be due to unresolved bed topography. This reinforces that an inversion model solving for both basal slip  
120 and bed topography could be used to overcome the shortcoming.

Cheng and Lötstedt [29] explore the sensitivity of modelled free surfaces in

ice flows to their basal topography and basal friction. They compare results from both the full Stokes model and the SSA. To compute the sensitivities, they use the adjoint equations to compute gradients for the perturbed data with  
125 respect to the basal conditions. They found that the sensitivity depended on the wavelength of the perturbation and its distance to the grounding line (the location where the ice sheet transitions from land to floating). As expected, changes in the topography can be directly seen in the surface whereas changes in the friction coefficient are more subtle.

130 An overview of the governing ice flow model used is given in Sect. 2. Section 3 goes through the construction of synthetic glacier surfaces for a number of different cases and then gives the methodology and algorithms needed for the inverse problem. The results of implementing the inverse method are given in Sect. 4 and additionally, a brief sensitivity analysis of these results to noise in  
135 surface data is covered in Subsec. 4.3. Finally, the results are discussed in Sect. 5 and final conclusions drawn in Sect. 6.

## 2. Governing equations

Beginning from the full Stokes flow equations for an ice sheet, conservation of mass for an incompressible fluid gives

$$\nabla \cdot \vec{u} = 0 \quad (1)$$

and conservation of momentum gives

$$\rho \frac{D\vec{u}}{Dt} = -\nabla p + \nabla \cdot \boldsymbol{\tau} + \vec{f} \quad (2)$$

where  $\frac{D}{Dt} \equiv \frac{\partial}{\partial t} + \vec{u} \cdot \nabla$  is the material derivative,  $\vec{u}$  is the flow velocity of the ice sheet,  $\rho$  the density,  $p$  the pressure,  $\nabla \cdot$  the divergence,  $\boldsymbol{\tau}$  the deviatoric stress  
140 tensor, and  $\vec{f}$  the body forces experienced by the ice sheet, namely gravity.

Pairing these conservation equations with the tensorial form of Glen and Nye's rheological law to describe the relationship between strain and shear [30, 31]

$$\dot{\gamma} = A(T) |\boldsymbol{\tau}|^{\frac{n-1}{2}} \boldsymbol{\tau}, \quad (3)$$

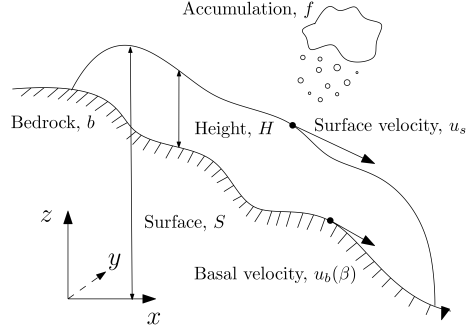


Figure 1: Ice sheet flowing downstream with surface  $S$ , bedrock  $b$ , and height  $H$ . The accumulation  $f$  is indicated by falling precipitation. Surface speed,  $u_s$ , and basal slip,  $\beta$ , are also indicated.

the conservation equations for ice flow in this paper (presented in Subsec. 2.1) can be derived. Here  $\dot{\gamma}$  is the strain rate tensor,  $A(T)$  is a temperature dependent constant, and  $|\boldsymbol{\tau}|$  denotes the second invariant. Classically, the flow of ice is assumed to be well described for  $n = 3$ .

### 145 2.1. Shallow ice approximation (SIA)

Under shallow-ice assumptions, the constitutive equations reduce to the SIA giving ice thickness evolution over time. From this thickness profile, the surface speed can be subsequently recovered. The SIA is chosen due to its relative simplicity. Typically the coordinate system is set up with the  $x$ -direction along the flow, the  $y$ -direction across the flow, and the  $z$ -direction aligned to the gravitational field. To simplify the testing of the new inversion method, the SIA is restricted to the unidirectional case. See Fig. 1 for a pictorial description of standard SIA notation.

The ice sheet height,  $H$ , is related to the surface  $S$  and the bedrock elevation  $b$  via

$$H = S - b \quad (4)$$

at any time,  $t$ . By considering the momentum balance, volume flux, and mass

conservation of the ice sheet, the SIA expression for ice thickness evolution is

$$\frac{\partial H}{\partial t} = f - \nabla \cdot \vec{q}, \quad (5)$$

where  $f$  is the accumulation/ablation function for the ice sheet in meters of water equivalent per year, and

$$\vec{q} = \int_b^S \vec{u} \, dz \quad (6)$$

describes the ice flux by integrating the velocity of the ice along the  $x$ -direction,  $u_x$ , from the bedrock to the free surface. Following [16] and adapting to include basal slip velocity  $u_b$ , the velocity profile is given by

$$\vec{u}(z) = \frac{1}{2} A (\rho g)^3 \|\nabla S\|_2^2 \nabla S [(S - z)^4 - H^4] + \vec{u}_b, \quad (7)$$

where  $\|\cdot\|_2$  is the regular  $L2$ -norm,  $\nabla S = \left(\frac{\partial S}{\partial x}, \frac{\partial S}{\partial y}\right)$ ,  $\rho$  is the ice density,  $g$  is the acceleration due to gravity and  $A$  Glens' flow parameter. Values for these constants are given in Table 1. The value for  $\rho$  is taken as the midpoint of the range for ice sheets as recommended by Cuffey and Paterson [19, Table 2.1]. The value for  $A$  given in Table 1 is for an ice sheet at  $-5 \text{ deg } C$  and was recommended by Cuffey and Paterson [19, Table 3.4].

The no-slip condition classically imposed [13, 14, 15, 16, 17] forces  $\vec{u}_b = 0$  for the ice sheet. This reduces the amount of surface data required for the inverse problem as without slip the system has only one unknown to recover. However, as discussed in the introduction, basal slip can have significant effect on ice height which reduces the practical applications if it is neglected. Here, no such condition is imposed and the ice sheet is allowed to have variable basal slip along the base of the flow.

Weertman [32] first proposed a power-type law for basal shear on a hard bed and both Fowler [9] and Lliboutry [33] proposed a more general form of the law for a flow with cavity formation. Budd et al. [34] found this generalised form to be empirically true for ice flow with basal shear described by

$$\vec{\tau}_b^3 = \frac{1}{A_s} \vec{u}_b, \quad (8)$$



where  $\vec{\tau}_b$  is the basal shear stress,  $A_s$  the sliding constant given in Table 1, and  $\vec{u}_b$  the basal velocity. The value for  $A_s$  is taken from [16].

Pairing this relation with the expression for basal shear from the full derivation of the SIA gives

$$\tau_b = -\rho g H \nabla S, \quad (9)$$

which combines with eq. (8) to give the following expression for basal velocity

$$\vec{u}_b = -\beta A_s (\rho g)^3 H^3 \|\nabla S\|_2^2 \nabla S, \quad (10)$$

where  $\beta(x, y)$  is the basal slip distribution which regulates the amount of basal slip at the ice base. Basal slip is restricted such that  $\beta(x) \in [0, 1]$  for all  $x$  in the ice sheet domain. Physically,  $\beta(x) = 0$  represents a sticky base and  $\beta(x) = 1$  a friction-less base. It is not required for  $\beta(x)$  to be constant along the ice sheets length.

Combining eqns. (7) and (10) gives a full expression for the velocity profile. This velocity profile is substituted into eq. (6) to give the ice flux. Finally, substituting this ice flux into the mass balance gives a non-linear diffusion equation

$$\frac{\partial H}{\partial t} = f - \nabla (D \nabla S) \quad (11)$$

with non-linear effective diffusion coefficient  $D$  given by

$$D = \frac{2}{5} A (\rho g)^3 \|\nabla S\|_2^2 H^4 \left( H + \frac{5}{2} A_r \beta \right), \quad (12)$$

where  $A_r$  is the ratio  $\frac{A_s}{A}$ . Note that the full velocity profile easily gives an expression for the surface velocity by setting  $z = S$ :

$$\vec{u}_s = -\frac{1}{2} A (\rho g)^3 \|\nabla S\|_2^2 H^3 (H + 2A_r \beta) \nabla S. \quad (13)$$

### 3. Inverse problem methodology

To begin considering the inverse problem, a methodology is first needed to produce synthetic surface data for a variety of test cases. The approach used for

Table 1: Typical values of constants used throughout.

Symbol	Name	Value
$A_s$	Sliding coefficient	$5 \times 10^{-14} \text{m}^8 \text{N}^{-3} \text{yr}^{-1}$
$A$	Glen’s law parameter	$4.16 \times 10^{-17} \text{Pa}^{-3} \text{yr}^{-1}$
$\rho$	Ice density	$880 \text{kg m}^{-3}$
$g$	Gravitational acceleration	$9.81 \text{m s}^{-2}$

this is outlined in Subsec. 3.1. Once these synthesised surfaces are produced, the inverse methodology can be applied. The approach used for the inverse problem requires two distinct stages; (1)  $S \rightarrow D$ , and (2),  $(D, u_s) \rightarrow (H, \beta)$ , which are described in Subsec. 3.2 and 3.3 respectively.

The full process described above is outlined in Fig. 2. Results of applying this process for each test case as given in the next section, Sec. 4.

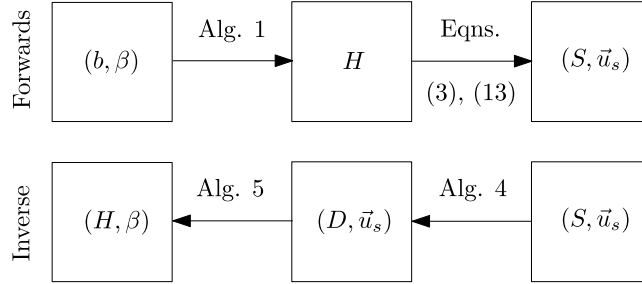


Figure 2: Problem approach with two main phases; (1) forwards, and (2) inverse.

### 3.1. Synthetic data generation

To model the ice surface, eq. (11) needs to be solved. There are numerous ways to approach this sort of time dependent diffusion problem and here we use a finite element methodology. First, eq. (11) is converted into a variational equation following from Langtangen and Logg [35] in Subsec. 3.1.1. The variational equation is solved numerically at each time-step until a steady state ice thickness

is reached. This steady state ice thickness is then added to the input bedrock to  
 190 give a steady state ice surface. Some example surfaces are given in Subsec. 3.1.2.

### 3.1.1. Formulation as a variational problem

First, a backward Euler discretization is used on the time derivative in eq. (11) to get

$$\frac{H^{n+1} - H^n}{\Delta t} = \nabla(D\nabla S)^{n+1} + f^{n+1}. \quad (14)$$

Arranging the unknowns to the left gives

$$H^{n+1} - \Delta t \nabla(D\nabla S)^{n+1} = H^n + \Delta t f^{n+1}. \quad (15)$$

Next, multiply the above through by a test function  $v \in \hat{V}$ , where the test space  $\hat{V}$  is defined as

$$\hat{V} = \{v \in H^1(\Omega) \quad : \quad v = 0 \text{ on } \partial\Omega\}, \quad (16)$$

such that the test function,  $v$ , vanishes on the boundary. The space,  $H^1(\Omega)$  is the Sobolev space containing functions  $v$  such that  $v^2$  and  $\|\nabla v\|_2^2$  have finite integrals over the domain  $\Omega$ . Taking eq. (16) and integrating over the domain gives

$$\int_{\Omega} H^{n+1} v \, dx - \Delta t \int_{\Omega} \nabla(D\nabla S)^{n+1} v \, dx = \int_{\Omega} (H^n + \Delta t f^{n+1}) v \, dx \quad (17)$$

where  $dx$  denotes the differential element for integration over the domain  $\Omega$ . Considering only the second order term and applying Green's first identity,

$$- \int_{\Omega} \nabla \cdot (D\nabla S) v \, dx = \int_{\Omega} D\nabla S \cdot \nabla v \, dx - \int_{\partial\Omega} D \frac{\partial S}{\partial n} v \, ds \quad (18)$$

where  $\partial\Omega$  is the boundary of  $\Omega$ ,  $\frac{\partial S}{\partial n} = \vec{n} \cdot \nabla u$  is the derivative of  $S$  in the outward unit normal direction,  $\vec{n}$ , and  $ds$  denotes the differential element for integration over the boundary of  $\Omega$ . Since the test function,  $v$ , is required to vanish on the boundary  $\partial\Omega$ , the second term vanishes also giving

$$\int_{\Omega} H^{n+1} v \, dx + \Delta t \int_{\Omega} D^{n+1} \nabla S^{n+1} \cdot \nabla v \, dx = \int_{\Omega} (H^n + \Delta t f^{n+1}) v \, dx. \quad (19)$$

Hence, our final weak form of eq. (11) is

$$F(H; v) := \int_{\Omega} H v + \Delta t D \nabla S \nabla v - (H^n + \Delta t f) v \, dx = 0 \quad (20)$$

where all functions are evaluated at the  $n + 1$  time step unless otherwise stated. By requiring this weak form to hold for all  $v \in \hat{V}$ , the problem of finding some  $H \in V$ , the trial-space, is well defined. Hence, the proper problem statement in weak form is: find  $H \in V$  such that

$$F(H; v) = 0 \quad \forall v \in \hat{V} \quad (21)$$

where

$$\hat{V} = \{v \in H^1(\Omega) \quad : \quad v = 0 \text{ on } \partial\Omega\}, \quad (22)$$

$$V = \{v \in H^1(\Omega) \quad : \quad v = H_D \text{ on } \partial\Omega\}. \quad (23)$$

To approximate the solution to this continuous problem, the infinite dimensional spaces  $V$  and  $\hat{V}$  are replaced with discrete, finite dimensional trial and test spaces,  $V_h \subset V$  and  $\hat{V}_h \subset \hat{V}$ . The discrete problem is then: find  $H_h \in V_h \subset V$  such that

$$F(H_h; v_h) = 0 \quad \forall v_h \in \hat{V}_h \subset \hat{V}. \quad (24)$$

This variational problem, together with suitable choices of function spaces  $V_h$  and  $\hat{V}_h$ , uniquely defines the approximate solution  $H_h$  to eq. (11).

### 3.1.2. Numerical computations and test case classification

195      A simple time stepping iteration is implemented to compute the steady state  
ice profile as described in Alg. 1. The weak problem, eq. (20), is solved using  
the open source finite element computational software library, FEniCS [36, 37].  
FEniCS provides a large library of finite elements and numerical solvers. In this  
study,  $P1$  elements are used for both spaces and the systems are solved using a  
200      GMRES linear solver, which is part of the PETSc package [38, 39, 40].

For all test cases, the accumulation/ablation function,  $f$  is defined as

$$f(x) = \begin{cases} f_0 \left(1 - \frac{300-x}{100}\right) & \text{if } x \leq 300 \\ f_0 \left(\frac{2200-x}{1900}\right) & \text{if } x \geq 300 \end{cases} \quad (25)$$

where  $f_0$  is the maximum value of the accumulation/ablation function and set to 0.5 for all future calculations. Adjusting this maximum values simply raises or lowers the steady state surface [41]. This function gives the most accumulation at the top end of the glacier and then linearly decreases along it's length until  
205 at the bottom end which has net ablation.

The bedrock and basal slip profiles are each chosen from three classes and there are three cases for each class. Equations which describe these profiles are given below in the lists following. For each class, the parameter changed to give a new case is  $\gamma$ . This may change the slope, extent or height dependent on the  
210 equation.

The bedrock profiles are given by;

1. Inclined. Denoted by  $b_1$ , and defined by

$$b(x) = (4500\gamma) - \gamma x,$$

where changing  $\gamma$  changes the slope and taken from  $\gamma \in \{0.15, 0.2, 0.25\}$ .

2. Bump. Denoted by  $b_2$ , and defined by

$$b(x) = 900 - 0.2x + \gamma \left( 50e^{\frac{-(x-2000)^2}{300^2}} \right)$$

where changing  $\gamma$  affects the bump height,  $\gamma \in \{1, 2, 3\}$ .

3. Undulations. Denoted by  $b_3$ , and defined by

$$b(x) = 900 - 0.2x + \gamma \left( -40e^{\frac{-(x-1300)^2}{300^2}} + 60e^{\frac{-(x-3100)^2}{400^2}} \right)$$

where  $\gamma$  again dictates bump height and  $\gamma \in \{1, 2, 3\}$ .

215 The basal slip profiles are given by;

1. Constant. Denoted by  $\beta_1$ , and defined by

$$\beta(x) = \gamma,$$

with  $\gamma \in \{0, 0.5, 1\}$ .

2. Gaussian. Denoted by  $\beta_2$ , and defined by

$$\beta(x) = e^{-\left(\frac{x-2500}{\gamma}\right)^{10}}$$

where changing  $\gamma$  affects the bump extent,  $\gamma \in \{500, 1000, 1500\}$ .

3. Switch. Denoted by  $\beta_3$ , and defined by

$$\beta(x) = \left(\frac{1}{2} + \frac{1}{2} \operatorname{erf}\left(\frac{x-2500}{\gamma}\right)\right)$$

where  $\gamma$  again changes the extent and  $\gamma \in \{500, 1000, 1500\}$ .

Going forward, the particular combination of bedrock and basal slip profiles  
 220 paired to produce a case of synthetic test data will be denoted by  $(b, \beta)$  with  
 subscripts giving the class of profile and the superscripts the particular case (by  
 selection of  $\gamma$ ). Visualisation of each profile is given in Fig. 3.

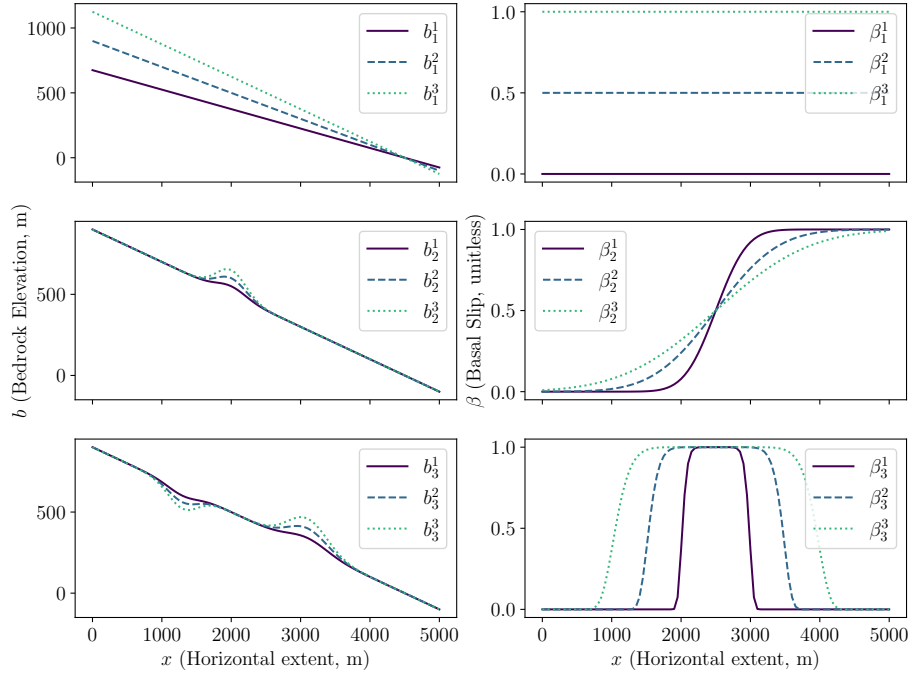


Figure 3: Graphical representation of the different bedrock and slip profiles which give rise to separate synthetic test cases.

Modelled steady state ice thickness profiles for given bedrock and slip profiles match the previous literature [41, 42, 16, 43] which were computed using finite difference schemes. The scheme is mesh independent as is clear in Fig. 4. Henceforth, all steady state profiles plotted and used are computed on a mesh with  $\Delta x = 20$  and  $\Delta t = 10^{-2}$ . A selection of steady state profiles is given below in Fig. 5 to illustrate effects observed at the surface due to changing basal conditions.

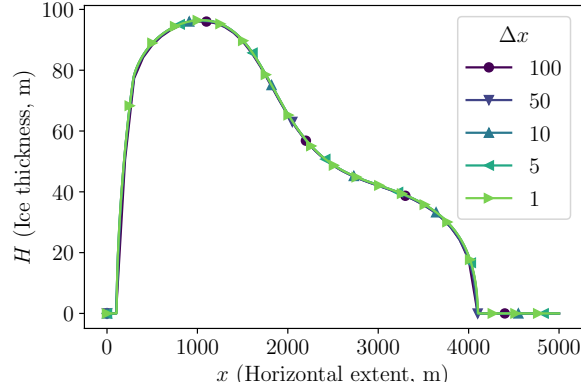


Figure 4: Steady state ice thickness in the forwards problem for  $b_1^1$  together with  $\beta_2^1$  for different values of  $\Delta x$  as indicated in the legend.

### 3.2. Recovery of $D$ from surface data

To recover the diffusion coefficient,  $D$ , from data an optimisation approach is used. This approach to minimise the error between observations of the surface and the one modelled using the recovered  $D$ . Hence the optimal control problem is to minimise the objective functional

$$\mathcal{J}(S, D) = \mathcal{J}_{mis} + \mathcal{J}_{reg} \quad (26)$$

$$= \frac{1}{2} \int_{\Omega} \|S_{\text{obs}} - S\|_2^2 d\Omega + \alpha \int_{\Omega} \|\nabla D\|_2^2 d\Omega \quad (27)$$

---

**Algorithm 1** FORWARDS SIA

---

1. Set  $H^0 = 0$  and  $n = 0$ .
2. Compute  $H$  such that

$$F(H; v) = \int_{\Omega} H v + \Delta t D(H) \nabla H \nabla v - [H^n + \Delta t f] v \, dx = 0$$

To ensure  $H \geq 0$ , set  $H^{n+1} = \max\{0, H\}$ .

If  $H_{\Delta} = \frac{H^{n+1} - H^n}{\Delta t} < 10^{-1}$ , set  $H^* = H^{n+1}$  and GOTO 3.

Otherwise, set  $n = n + 1$ , REPEAT 2.

3. Finally compute  $S^*$  and  $\mathbf{u}_s^*$  via

$$\begin{aligned} S^* &= H^* + b, \\ \mathbf{u}_s^* &= -\frac{1}{2} A(\rho g)^3 \|\nabla S^*\|_2^2 H^{*3} \left( H^* + 2 \frac{A_s}{A} \beta \right) \nabla S^*. \end{aligned}$$


---



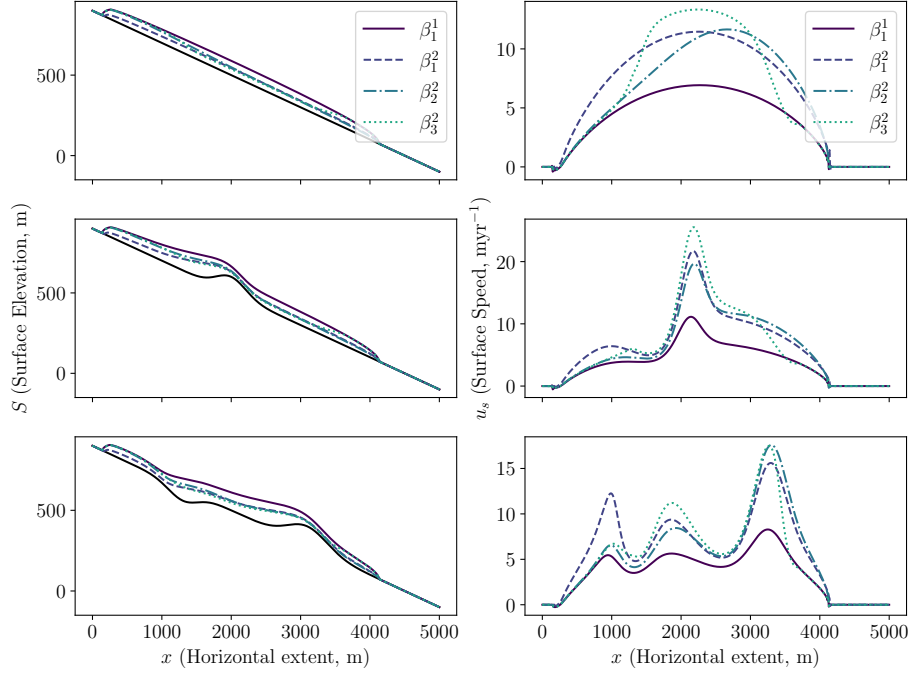


Figure 5: Left: resultant steady state ice surfaces for different slip regimes (indicated by line-style/colour in the plot legend) paired together with different bedrock profiles (indicated in black beneath the plotted surfaces) . Right: corresponding surface speed,  $u_s$  for each steady state surface..

with respect to  $D$  subject to

$$-\nabla(D\nabla S) = f \quad (28)$$

$$S = S_{\text{obs}} \text{ on } \Gamma \quad (29)$$

$$\Omega = [x_s, x_f] \quad (30)$$

$$\Gamma = (x_s) \cup (x_f) \quad (31)$$

where  $x_s$  and  $x_f$  demarcate the start and end of the ice domain. The Tikhonov regularisation term,  $\mathcal{J}_{reg}$ , is necessary to ensure that the problem is well-posed for poor initial conditions or data. The Tikhonov term can be thought of as a cost term for the gradient of the control; essentially the larger  $\alpha$ , the more

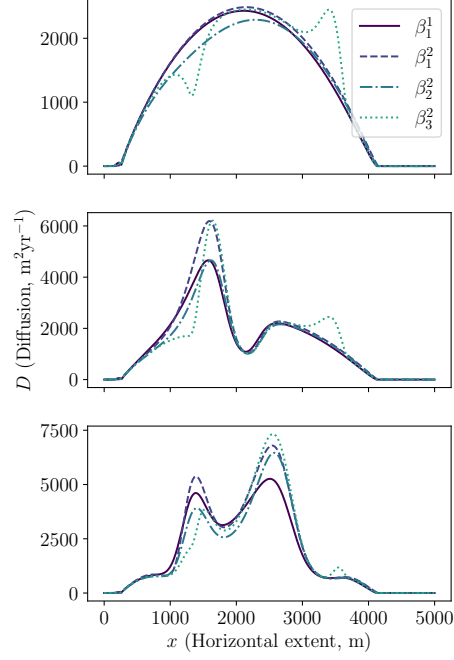


Figure 6: Effect of different slip regimes on the steady state diffusion.

235 favourable a smooth solution is.

The PDE constraint  $-\nabla(D\nabla S) = f$  can equivalently be considered as a residual constraint  $e(D, S) = 0$  where  $e(D, S)$  is defined by the residual equation (in the weak sense):

$$(\nabla e(D, S), \nabla \phi) = (D\nabla S, \nabla \phi) - (f, \phi) \quad \forall (D, S) \in K \times V, \quad \phi \in V \quad (32)$$

where

$$V = H^1(\Omega),$$

$$K = \left\{ D \in L^1(\Omega); \quad \int_{\Omega} \|\nabla D\|_2 \, d\Omega < \infty \text{ and } \alpha_1 \leq D \leq \alpha_2 \text{ a.e. in } \Omega \right\}.$$

To minimise the objective, an augmented Lagrangian approach is used. This enables relaxation of the residual constraint  $e(D, S)$  which enhances the convexity of the objective functional. To do this, the augmented Lagrangian functional,

$\mathcal{L}_r : K \times V \times V \rightarrow R$ , is introduced:

$$\mathcal{L}_r(D, S; \mu) = \mathcal{J}(D, S) + (\nabla \mu, \nabla e(D, S)) + \frac{r}{2} \|\nabla e(D, S)\|_2^2 \quad (33)$$

where  $r \geq 0$  is a given constant and  $R$  denotes the reals. Finding the saddle point of this augmented form is equivalent to finding a minimum of the objective functional [e.g. 44, 45].

Following from [44], the augmented Lagrangian is discretised. Taking  $V_h$  as the standard piecewise linear finite element space, the discrete form,  $L_r : K_h \times \mathring{V}_h \times \mathring{V}_h \rightarrow R$ , is given by

$$L_r(D_h, S_h; \mu_h) = J_h(D_h, S_h) + (\nabla \mu_h, \nabla e_h(D_h, S_h)) + \frac{r}{2} \|\nabla e_h(D_h, S_h)\|_2^2, \quad (34)$$

where

$$D_h \in K_h = K \cap V_h, \quad S_h \in \mathring{V}_h = V_h \cap H^1(\Omega), \quad (35)$$

with

$$J_h(D_h, S_h) = \frac{1}{2} \int_{\Omega} \|S^{\text{obs}} - S_h\|_2^2 d\Omega + \alpha \int_{\Omega} \|\nabla D_h\|_2^2 d\Omega. \quad (36)$$

Taking the discrete form of the residual equation (32),  $e_h(D_h, S_h) \in \mathring{V}_h$  is defined as the solution to

$$(\nabla e_h(D_h, S_h), \nabla \phi) = (D_h \nabla S_h, \nabla \phi_h) - (f, \phi_h), \quad \forall \phi_h \in \mathring{V}_h \quad (37)$$

for any  $(D_h, S_h) \in K_h \times \mathring{V}_h$ . It can be shown (see e.g. [45]) that for any  $r \geq 0$ ,  
 240 there exists at least one saddle point of  $L_r$  which can be found using a simple Uzawa type algorithm given in Alg. 2. This basic form of the algorithm is convergent for choices of  $0 < \rho_r < r$  [45].

To perform the minimisation in Alg. 2 (eq. (38)), an alternative iteration is used, first computing  $S_h$  and then the corresponding  $D_h$ . As in [44], this is  
 245 referred to as the modified Uzawa algorithm and is given explicitly in Alg. 3. Step 2 of this modified form still requires two minimisations steps. The following

---

**Algorithm 2** BASIC UZAWA

---

Choose  $r \geq 0$  and  $\rho_r < r$ . Given  $\lambda_0 \in \mathring{V}_h$ , iterate through  $n$  by computing the pair  $\{D_h, S_h\} \in$  such that

$$L_r(D^n, S^n; \lambda^n) = \min\{L_r(p, v; \lambda^n) \quad \forall (p, v) \in K_h \times \mathring{V}_h\} \quad (38)$$

and then updating  $\lambda^{n+1}$  via

$$\lambda^{n+1} = \lambda^n + \rho_r e_h(D^n, S^n). \quad (39)$$


---

---

**Algorithm 3** MODIFIED UZAWA

---

Choose  $r \geq 0$  and  $\rho_r < r$ . Given  $\lambda_0 \in \mathring{V}_h$  and  $D^0 \in K_h$ . Set  $n = 1$ .

1. Set  $k = 1$  and  $D_0^n = D^{n-1}$ .
2. Compute  $S_k^n \in \mathring{V}_h$  by solving

$$L_r(D_{k-1}^n, S_k^n; \lambda^{n-1}) = \min_{v_h \in \mathring{V}_h} L_r(D_{k-1}^n, v_h; \lambda^{n-1}) \quad (40)$$

and then compute  $D_n^k \in V_h$  by solving

$$L_r(D_k^n, S_k^n; \lambda^{n-1}) = \min_{p_h \in V_h} L_r(p_h, S_k^n; \lambda^{n-1}) \quad (41)$$

Compute  $D_k^n = \max\{\alpha_1, \min\{D_k^n, \alpha_2\}\}$ .

If  $\|D_k^n - D_{k-1}^n\|_2 \leq \epsilon_q$  OR  $k \geq k_{\max}$ , set  $S^n = S_k^n$  and  $D^n = D_k^n$ , GOTO 3.

Otherwise, set  $k = k + 1$ , GOTO 2.

3. Compute  $\lambda^n$  by

$$\lambda^n = \lambda^{n-1} + \rho_r e_h(D^n, S^n). \quad (42)$$

If  $\|S^n - S^{\text{obs}}\|_2 \leq \epsilon_S$  OR  $n \geq n_{\max}$ , END.

Otherwise, set  $n = n + 1$ , GOTO 1.

---

will show that each minimisation (eq. (40) and eq. (41)) is equivalent to solving a system of variational equations, which FEniCS is capable of solving.

The Gateaux derivative of  $\mathcal{L}_r$  with respect to  $S_h$  in the direction  $w_h$  is given by

$$\mathcal{L}'_r(D_h, S_h; \lambda_h)w_h = (S_h - S^{\text{obs}}, w_h) + (D_h \nabla \lambda_h, \nabla w_h) + r(D_h \nabla e_h, \nabla w_h). \quad (43)$$

To minimise  $\mathcal{L}_r$ , we solve the above two equations as a system by setting eq. (43) to 0:

$$0 = \mathcal{L}'_r(D_h, S_h; \lambda_h)w_h, \quad (44)$$

$$0 = (S_h - S^{\text{obs}}, w_h) + (D_h \nabla \lambda_h, \nabla w_h) + r(D_h \nabla e_h, \nabla w_h). \quad (45)$$

Recall that  $e_h(D_h, S_h)$  is the solution to

$$(\nabla e_h(D_h, S_h), \nabla \phi) = (D_h \nabla S_h, \nabla \phi) - (f, \phi).$$

Hence, arranging the known variables to the left (terms not involving either of  $e_h$  or  $S_h$ ) our minimisation is equivalent to finding  $(S_h, e_h) \in \mathring{V}_h \times \mathring{V}_h$  such that

$$(S_h, w_h) + r(D_h, \nabla e_h, \nabla w_h) = (z, w_h) - (D_h \nabla \lambda_h, \nabla w_h) \quad (47)$$

$$(\nabla e_h(D_h, S_h), \nabla \phi_h) = (D_h \nabla v_h, \nabla \phi_h) - (f, \phi_h), \quad (48)$$

$\forall w_h \in \mathring{V}_h$  and  $\forall \phi_h \in \mathring{V}_h$ .

Similarly, the Gateaux derivative of  $\mathcal{L}_r$  with respect to  $D_h$  in the direction  $p_h$  is given by

$$\mathcal{L}'_r(D_h, S_h; \lambda_h)p_h = \alpha(\nabla D_h, \nabla p_h) + (p_h \nabla S_h, \nabla \lambda_h) + r(p_h \nabla S_h, \nabla e_h) \quad (49)$$

where  $e_h$  is the solution to eq. (32) as above. As above, setting eq. (49) to 0 and arranging unknowns to the left gives the system which can be solved to find  $D_h$  which minimises  $\mathcal{L}_r$  with respect to  $D_h$ . The problem is then to find  $(D_h, e_h) \in V_h \times \mathring{V}_h$  such that

$$\alpha(\nabla D_h, \nabla p_h) + r(p_h \nabla S_h, \nabla e_h) = -(p_h \nabla S_h, \nabla \lambda_h), \quad (50)$$

$$(\nabla e_h, \nabla \phi_h) - (D_h \nabla v_h, \nabla \phi) = -(f, \phi_h), \quad (51)$$

250  $\forall p_h \in V_h$  and  $\forall \phi_h \in \mathring{V}_h$ . Hence, the two minimisation problems in Step 2 of Alg. 3 can be expressed as solving two systems as is outlined in Alg. 4.

### 3.3. Subsequent recovery of $(H, \beta)$ from $D$

Once  $D$  is recovered via the Uzawa algorithm above, one more step is required to recover the ice thickness and basal slip. This is to find  $(H, \beta)$  given  $(D^{\text{inv}}, u_s^{\text{obs}})$ . To do this, the SIA expressions for  $D$  and  $\mathbf{u}_s$  are needed. Recall that these were

$$0 = D - K \|\nabla S\|_2^2 H^4 (H + \frac{5}{2} A_r \beta) \quad (58)$$

$$0 = \vec{u}_s - \left[ \frac{-5}{4} K \|\nabla S\|_2^2 H^3 (H + 2A_r \beta) \right] \nabla S \quad (59)$$

where  $K = 2/5A(\rho g)^3$ ,  $A_r = A_s/A$ ,  $\|\nabla S\|_2^2 = \left(\frac{\partial S}{\partial x}\right)^2 + \left(\frac{\partial S}{\partial y}\right)^2$ . Since the velocity has two-components, this is a system of three equations with two unknowns. To reduce this to a system of two equations with two unknowns, the two-norm of the velocity is taken. The velocity equation is therefore,

$$0 = \|\vec{u}_s\|_2 - \left[ \frac{5}{4} K \|\nabla S\|_2^2 H^3 (H + 2A_r \beta) \right] \|\nabla S\|_2 \quad (60)$$

which can be rearranged to give

$$\beta = \frac{1}{2A_r} \left( \frac{\|\vec{u}_s\|_2}{\frac{5}{4} K \|\nabla S\|_2^2 H^3 \|\nabla S\|_2} - H \right). \quad (61)$$

Now, substituting this into the equation involving  $D$  gives

$$0 = D - K \|\nabla S\|_2^2 H^4 \left( H + \frac{5}{2} A_r \left( \frac{1}{2A_r} \left( \frac{\|\vec{u}_s\|_2}{\frac{5}{4} K \|\nabla S\|_2^2 H^3 \|\nabla S\|_2} - H \right) \right) \right) \quad (62)$$

$$0 = D - \frac{\|\vec{u}_s\|_2}{\|\nabla S\|_2} H + \frac{1}{4} K \|\nabla S\|_2^2 H^5 \quad (63)$$

Using this final form, it is clear that recovering  $H$  is as simple as solving for the zeroes of the quintic

$$p(H) = \frac{1}{4} K \|\nabla S\|_2^2 H^5 - \frac{\|\vec{u}_s\|_2}{\|\nabla S\|_2} H + D. \quad (64)$$

---

**Algorithm 4** MODIFIED UZAWA (SYSTEM VERSION)

---

Choose  $r \geq 0$  and  $\rho_r < r$ . Given  $\lambda_0 \in \mathring{V}_h$  and  $D^0 \in K_h$ . Set  $n = 1$ .

1. Set  $k = 1$  and  $D_0^n = D^{n-1}$ .
2. Compute the pair  $(S_n^k, e_h) \in \mathring{V}_h \times \mathring{V}_h$  by solving

$$(S_k^n, w_h) + r(D_{k-1}^n, \nabla e_h, \nabla w_h) = (S^{\text{obs}}, w_h) - (D_{k-1}^n \nabla \lambda^{n-1}, \nabla w_h) \quad (52)$$

$$(\nabla e_h, \nabla \phi) = (D_{k-1}^n \nabla v_h, \nabla \phi) - (f, \phi), \quad (53)$$

and then compute  $(D_n^k, e_h) \in V_h \times \mathring{V}_h$  by solving

$$\alpha(\nabla D_k^n, \nabla p_h) + r(p_h \nabla S_k^n, \nabla e_h) = -(p_h \nabla S_k^n, \nabla \lambda^{n-1}), \quad (54)$$

$$(\nabla e_h, \nabla \phi) - (D_k^n \nabla v_h, \nabla \phi) = -(f, \phi). \quad (55)$$

Compute  $D_k^n = \max\{\alpha_1, \min\{D_n^k, \alpha_2\}\}$ .

If  $\|D_n^k - D_n^{k-1}\|_2 \leq \epsilon_q$  OR  $k \geq k_{\max}$ , set  $S^n = S_k^n$  and  $q^n = D_k^n$ , GOTO 3.

Otherwise, set  $k = k + 1$ , GOTO 2.

3. Compute  $\lambda^n$  by

$$\lambda^n = \lambda^{n-1} + \rho_r e_h(q^n, S^n) \quad (56)$$

where  $e_h(D^n, S^n)$  solves

$$(\nabla e_h(D^n, S^n), \nabla \phi) = (D^n \nabla S^n, \nabla \phi) - (f, \phi). \quad (57)$$

If  $\|D^n - D^{n-1}\|_2 \leq 10^{-3}$  OR  $n \geq n_{\max}$ , END.

Otherwise, set  $n = n + 1$ , GOTO 1.

---

To improve the efficiency of the numerical algorithm, the extrema of this polynomial are used. To find these, differentiate and set to zero,

$$p'(H_{ex}) = 0 = \frac{5}{4}K\|\nabla S\|_2^2 H_{ex}^4 - \frac{\|\vec{u}_s\|_2}{\|\nabla S\|_2}, \quad (65)$$

$$\implies H_{ex}^4 = \frac{\frac{\|\vec{u}_s\|_2}{\|\nabla S\|_2}}{\frac{5}{4}K\|\nabla S\|_2^2}, \quad (66)$$

$$\implies H_{ex} = \left( \frac{\|\vec{u}_s\|_2}{\frac{5}{4}K\|\nabla S\|_2^2\|\nabla S\|_2} \right)^{1/4}. \quad (67)$$

Note that  $H_{ex} \geq 0$  always. This extremum can be classified as a minimum or maximum by finding the sign of the second derivative,

$$p''(H) = \frac{20}{4}K\|\nabla S\|_2^2 H^3. \quad (68)$$

Since  $H_{ex} \geq 0$  it follows that  $p''(H_{ex}) \geq 0$  so the extremum is a local minimum.

Consider again  $\beta$  defined by the equation for  $\vec{u}_s$ . Since  $\beta \geq 0$  it follows that

$$0 \leq \frac{\|\vec{u}_s\|_2 - H(\frac{5}{4}K\|\nabla S\|_2^2\|\nabla S\|_2 H^3)}{\frac{10}{4}A_r K\|\nabla S\|_2^2\|\nabla S\|_2 H^3} \quad (69)$$

$$\implies 0 \leq \|\vec{u}_s\|_2 - H(\frac{5}{4}K\|\nabla S\|_2^2\|\nabla S\|_2 H^3) \quad (70)$$

$$\implies H^4 \leq \frac{\|\vec{u}_s\|_2}{\frac{5}{4}K\|\nabla S\|_2^2\|\nabla S\|_2} \quad (71)$$

$$\implies H \leq \left( \frac{\|\vec{u}_s\|_2}{\frac{5}{4}K\|\nabla S\|_2^2\|\nabla S\|_2} \right)^{1/4}. \quad (72)$$

In fact, when  $\beta = 0$ , precisely the abscissa of the minimum of  $p(H)$  is returned.

255 Hence, this abscissa is the maximum allowable value which  $H$  can take to give a viable solution. This notion can be used to restrict the search interval for roots of  $p(H)$  to  $H \leq H_{ex}$ . Additionally, if  $p(H_{ex}) \geq 0$ , there are no other viable roots (there is one negative root which is not allowed since  $H \geq 0$ ) and so  $H^* = H_{ex}$ . These processes are outlined in the modified Newton's algorithm given in Alg. 5.

#### 260 4. Numerical results

The results of this study are presented in two parts. The first relating to the recovery of the non-linear diffusion  $D$  in Subsec. 4.1, and the second covering



---

**Algorithm 5** MODIFIED NEWTONS

---

For each coordinate  $\mathbf{x}$  in  $\Omega$ :

Set  $j = 0$ .

1. Calculate  $H_{\max}$  by

$$H_{max} = \left( \frac{\|\vec{u}_s\|_2}{\frac{5}{4}K \|\nabla S\|_2^2 \|\nabla S\|_2} \right)^{1/4} \quad (73)$$

if  $p(H_{\max}) \geq 0$ , set  $h^* = H_{\max}$ . END.

Otherwise, GOTO 2.

2. Set  $n = 0$  and  $h^0 = H_{\max} - 5j$ .

(a) Set  $h^n = h^0$ .

(b) Compute  $h^{n+1}$  by

$$h^{n+1} = h^n - \frac{p(h^n)}{p'(h^n)} \quad (74)$$

(c) If  $p(h^{n+1}) \leq \epsilon_p$ , set  $h_{\text{newt}} = h^{n+1}$ . GOTO (3).

Otherwise, increment  $n = n + 1$ . GOTO (a).

3. If  $h_{\text{newt}} < 0$  or  $h_{\text{newt}} > H_{\max}$ , set  $j = j + 1$ . GOTO (2).

Otherwise, set  $h^* = h_{\text{newt}}$ . END.

---

the subsequent recovery of the pair  $(H^{\text{inv}}, \beta^{\text{inv}})$  from the pair  $(D^{\text{inv}}, u_s^{\text{obs}})$  in Subsec. 4.2. For each recovery, the errors are calculated by

$$\mathcal{E}_F = \frac{\|F^* - F^{\text{inv}}\|_2}{\|F^*\|_2}, \quad F \in \{D, H, \beta\}. \quad (75)$$

In the case where  $\beta \equiv \beta_1^1 = 0$ , the error is calculated as  $\mathcal{E} = \|\beta^{\text{inv}}\|_2$ .

#### 4.1. Recovery of $D$

In each implementation, the domain of the problem is  $\Omega = [x_s, x_f]$  where  $x_s$  is the location of the dome (first point after the onset of ice where  $\frac{\partial S}{\partial x} = 0$ ) and  $x_f$  is where the ice ends. The interval is split into uniformly distributed intervals of length  $1/nx$ . Unless otherwise specified,  $nx = 200$ . The augmented Lagrangian coefficient is set to  $r = 1$  and the initial guess for the Lagrange multiplier is  $\lambda^0 = 0$ . The lower and upper bounds used to constrain  $K$  are  $\alpha_1 = 10^{-2}$  and  $\alpha_2 = 10^5$ .

To solve the two systems of variational equations in Alg. 4, FEniCS is used again. For each test case, an initial guess of  $D^0 = 1000$  is paired with an initial regularisation  $\alpha = 10^0$ . Using these inputs, Alg. 4 is implemented with  $(n_{\text{max}}, k_{\text{max}}) = (20, 200)$  and  $\epsilon_S = 10^{-6}$ . Once this algorithm terminates,  $\alpha$  is reduced by a factor of 10 and the final solution,  $D^{\text{inv}}$ , is taken as an initial guess  $D^0$  to rerun Alg. 4. This process is repeated until the final error  $\|S - S^{\text{obs}}\|_2$ , is either no longer decreasing or  $\|S - S^{\text{obs}}\|_2 < \epsilon_S$ . Typically this occurs at around  $\alpha = 10^{-4}$ . Fig. 7 shows the recovered  $D^{\text{inv}}$  for 3 cases of bedrock of with the same slip:  $(b_1^2, \beta_2^2)$ ,  $(b_2^2, \beta_2^2)$ , and  $(b_3^2, \beta_2^2)$ . Table 2 gives the relative  $L_2$ -norm error between the exact parameter  $D^*$  and the recovery  $D^{\text{inv}}$  as calculated by eq. (75) for 12 distinct pairings of bedrock and basal slip.

#### 4.2. Recovery of $(H, \beta)$

Once  $D^{\text{inv}}$  is calculated, Alg. 5 is implemented to recover  $(H^{\text{inv}}, \beta^{\text{inv}})$ . Termination criteria for Newton's method is set as  $\epsilon_p = 10^{-2}$ .

Fig. 8 shows the recovered  $H^{\text{inv}}$  alongside the recovered  $\beta^{\text{inv}}$  for the same 3 cases of bedrock/slip as shown for  $D^{\text{inv}}$ :  $(b_1^2, \beta_2^2)$ ,  $(b_2^2, \beta_2^2)$ , and  $(b_3^2, \beta_2^2)$ . Table 3

Table 2: Relative error in  $D^{\text{inv}}$ ,  $\mathcal{E}_D$ , calculated by eq. (75). All values are  $\times 10^{-2}$ . Colouring indicates size of error (lighter shading is better) and additionally corresponds to the colour of sample solutions in Fig. 7.

$\mathcal{E}_D$	$\beta_1^1$	$\beta_1^2$	$\beta_2^2$	$\beta_3^2$
$b_1^2$	0.12	0.47	0.31	0.22
$b_3^2$	1.1	4.09	0.29	4.45
$b_3^2$	0.72	0.9	0.56	1.38

Table 3: Relative error in  $(H, \beta)^{\text{inv}}$ ,  $\mathcal{E}_{(H, \beta)}$ , calculated by eq. (75). All errors are  $\times 10^{-2}$ . Colouring indicates size of error (lighter shading is better) and additionally corresponds to the colour of sample solutions in Fig. 8.

$\mathcal{E}_H$	$\beta_1^1$	$\beta_1^2$	$\beta_2^2$	$\beta_3^2$
$b_1^2$	7.43	6.23	11.18	11.13
$b_3^2$	5.17	6.28	9.82	6.12
$b_3^2$	7.44	4.54	9.36	10.74

$\mathcal{E}_\beta$	$\beta_1^1$	$\beta_1^2$	$\beta_2^2$	$\beta_3^2$
$b_1^2$	101.31	19.43	4.97	0.49
$b_3^2$	142.36	21.31	8.53	15.98
$b_3^2$	79.63	19.68	5.1	2.41

(left) gives the relative  $L2$ -norm error between the exact parameter  $H^*$  and the recovery  $H^{\text{inv}}$  as calculated by eq. (75) for 12 distinct pairings of bedrock and basal slip.

#### 4.3. Sensitivity to noise in data.

To evaluate the robustness of the proposed methodology, random noise is added to the synthetic data to simulate noise in ice surface measurements and in estimations of the accumulation function. Noise is synthesised in the following

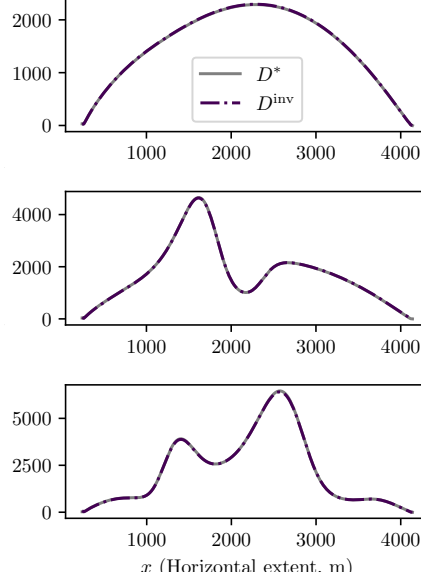


Figure 7: A selection of optimised  $D^{\text{inv}}$  from the algorithm. In all cases, the target bedrock is defined by  $b \equiv b_i^2$  and  $\beta \equiv \beta_2^2$ .

way;

$$F^\delta = F^{\text{obs}} + (1 + r_\delta) \|F^{\text{obs}}\|_2, \quad F \in \{S, f, u_s\} \quad (76)$$

$$r_\delta \sim N(0, \delta^2), \quad \delta \in [0, 1], \quad (77)$$

where,  $\delta$ , dictates the amount of noise added to the measurement. Before passing the noisy data into the algorithms, it is filtered as would be done in realistic applications. Here, this is simply done using a moving average with a window width of 200m.

Average relative errors in diffusion recovery for 100 random samples noisy data,  $S^\delta$  and  $f^\delta$ , are given in Tab. 4. Similarly, relative errors for subsequent ice thickness calculation with 50 samples of noisy surface speed,  $u_s^\delta$ , are also given in Tab. 4 (assuming  $D^{\text{inv}}$  calculated with no noise on  $S$  and  $f$ ).

In Fig. 9, the target solution,  $D^*$ , is plotted together with the solution envelopes for both  $S^\delta$  and  $f^\delta$ . Each envelope of solutions is calculated by taking the minimum and maximum solution for  $D^{\text{inv}}$  at each coordinate. This plot

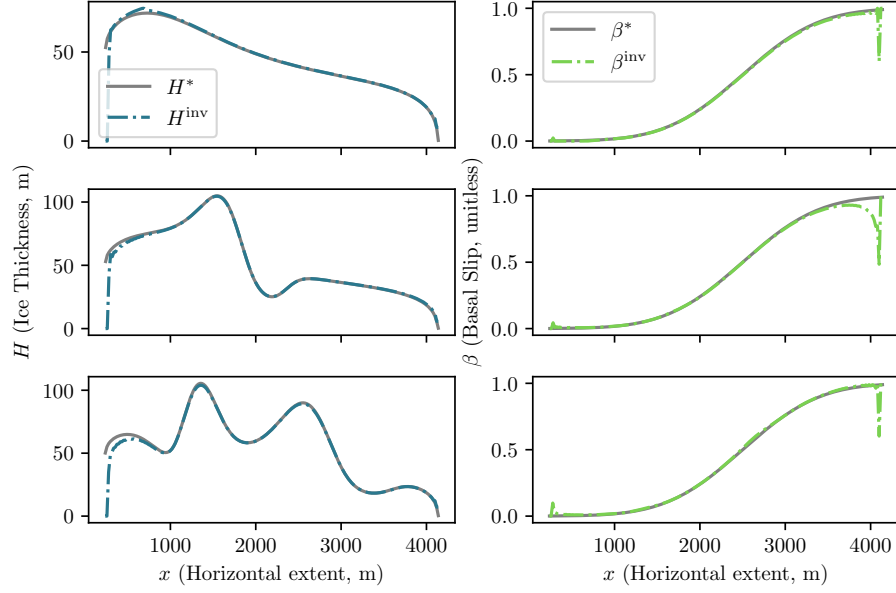


Figure 8: A selection of subsequent pairs  $(H^{\text{inv}}, \beta^{\text{inv}})$  using Alg. 5. In all cases, the target bedrock is defined by  $b \equiv b_i^2$  ( $i \in \{1, 2, 3\}$ ) and  $\beta \equiv \beta_2^2$ .

uses the same 50 samples as in Tab. 4. Fig. 10 shows the target ice thickness,  $H^*$  with the solution envelope for input  $u_s^\delta$ . In both figures, 10% error bands calculated by taking

$$F^* \pm 0.1F^* \quad F \in \{D, H\} \quad (78)$$

are shown. Additionally, the median solution is overlaid for each solution set.

## 5. Discussion

Results presented in Sec. 4 show that it is possible to use an augmented Lagrangian approach to recover the diffusion in the steady state SIA model from surface elevation data. Accuracy in the recovery without noise was high (with relative error in the magnitude of  $10^{-2}$  or less, see Tab. 2) and could subsequently produce good estimations of ice thickness and basal slip (relative

Table 4: Average relative error,  $\bar{\mathcal{E}}$ , calculated over 50 samples. For  $(S^\delta, f^\delta)$ ;  $\bar{\mathcal{E}}_D$ , and for  $u_s^\delta$ ;  $\bar{\mathcal{E}}_H$  are given. Error is calculated by eq. (75). Noise is added with  $\delta = 0.05$  (5% noise) for all entries. Colouring indicates size of error (lighter shading is better) and additionally corresponds the inversion envelope colour in Figs. 9 and 10.

$\times 10^{-1}$	$(b_1^2, \beta_1^2)$	$(b_2^2, \beta_2^2)$	$(b_3^2, \beta_3^2)$
$\bar{\mathcal{E}}_D(S^\delta)$	4.5	2.04	5.5
$\bar{\mathcal{E}}_D(f^\delta)$	0.04	0.06	0.16
$\bar{\mathcal{E}}_H(u_s^\delta)$	0.43	1.17	1.22

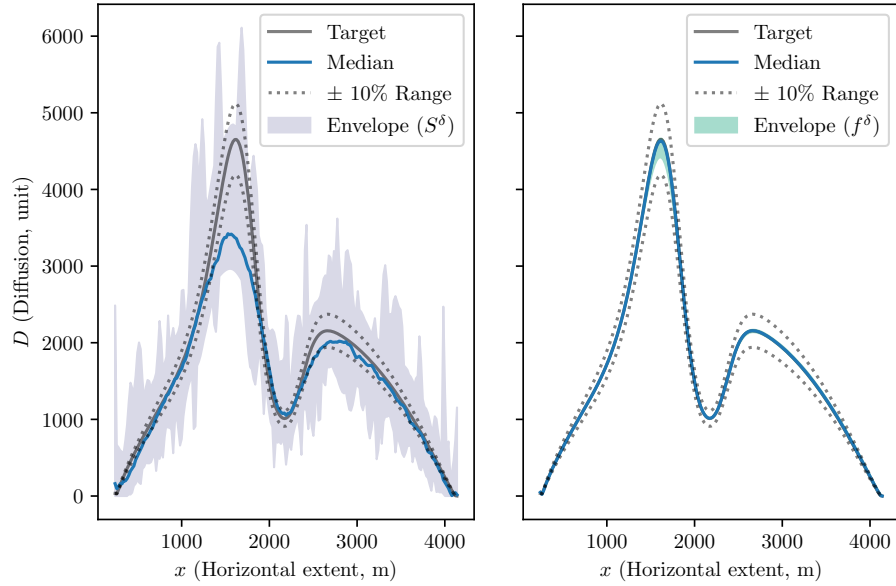


Figure 9: Envelope of 50 samples of recovered diffusion,  $D^{\text{inv}}$  for noisy input surface elevation,  $S^\delta$ , and wind accumulation,  $f^\delta$ . For both,  $\delta = 0.05$ . Case is  $(b_2^2, \beta_2^2)$ .

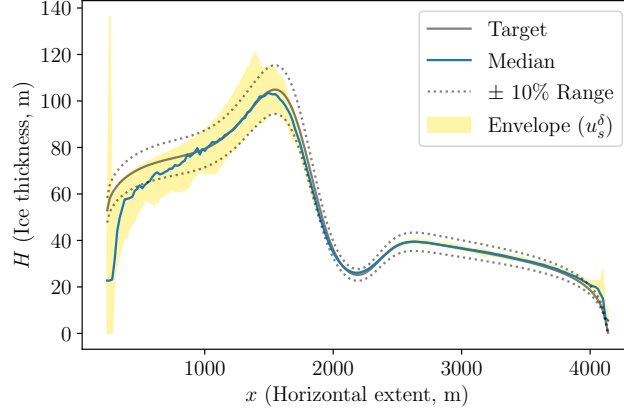


Figure 10: Envelope of 50 samples of recovered ice thicknesses,  $H^{\text{inv}}$ , for noisy input surface speed,  $u_s^\delta$ , with  $\delta = 0.05$ . Case is  $(b_2^2, \beta_2^2)$ .

error magnitude at most  $10^{-1}$ , see Tab. 3) by incorporating additional surface speed data.

Locations of largest error occur in parts of the domain where SIA assumptions breakdown, for example in locations of steeper underlying bedrock [22]. Errors also occur where computations become unstable, for example when  $\frac{\partial S}{\partial x} \rightarrow 0$  and  $u_s \rightarrow 0$ . This poses difficulty for application of the method to real data as these locations are often of most interest to geo-scientists as they can be the hardest to measure [1].

Initial sensitivity analysis presented in Subsec. 4.3 indicates that the method can be effective with some noise (5%) in some surface measurements.

The solution for  $D^{\text{inv}}$  is very good (mean errors of magnitude  $10^{-2}$ ) for noise in the accumulation function,  $f^\delta$ . This is a positive finding as this function can be hard to estimate in practice. For noise of surface elevation,  $S^\delta$ , the inversion is less successful, with errors of magnitude  $5 \times 10^{-1}$ . In this case, the method is replicating the bumpiness in the smoothed surface profile by having bumpiness in the solution for  $D^{\text{inv}}$ . A more advanced method of filtering the surface data could deal with much of this error but further analysis is needed. In the case of noisy surface speed,  $u_s^\delta$ , results are good for the ice thickness recovery with mean

errors of magnitude at most  $1.2 \times 10^{-1}$ . This is echoed in Fig. 10, with the noisy solution envelope falling between the 10% error bands almost everywhere.

325 Overall, the sensitivity results are promising for potential future uses of the method with noisy surface measurements as would be the case for field data.

Previous studies either; (a) disregard basal slip [42], or (b) require prior knowledge of the ice thickness in some locations [43]. The method presented here does not have such limitations.

330 Overall the method has performed well in the restricted, idealised cases tested in this paper. The main caveats in considering the applicability to real cases are the steady state assumption, the restriction to the unidirectional SIA model, and the wavelength of  $\beta$  considered.

Assumption of a steady state may not be valid for many ice sheets and glaciers. In these cases, a basic work around can be implemented as long as the ice surface is known at two time points, giving  $S_1$  and  $S_2$ , which allows the estimation

$$\frac{\partial H}{\partial t} = \frac{\partial S}{\partial t} \approx \frac{S_2 - S_1}{\Delta t}, \quad (79)$$

and changes the PDE constraint to

$$-\nabla(D\nabla S) = f' = f - \frac{S_2 - S_1}{\Delta t}. \quad (80)$$

This kind of approximation technique was used successfully by [42].

335 Secondly, the unidirectional SIA model is restricted to slow moving grounded ice which restricts the uses for this method. Accounting for limitations in the SIA model itself could be approached from a Bayesian framework as in Babaniyi et al. [3]. This would be particularly important when considering the confidence of inversions using real data.

340 Additionally, the unidirectional nature of the test cases allow for fast computation time. While results here indicate that the same methodology could be applied to a two dimensional case study, this may require more work as the augmented Lagrangian, while convergent, is computationally inefficient [46].



Finally, test cases in this paper all have basal slip distribution with variation  
 345 over large wavelengths. As Gudmundsson and Raymond [47] found, small  
 amplitude perturbations in basal slip could only be detected in the surface  
 measurements if the perturbation had a large wavelength in comparison with the  
 ice thickness. If the wavelength was too small, mixing occurred in the surface  
 data between basal slip and bedrock topography which could cause the inverse  
 350 method to fail in basal slip recovery. This restricts the ability of the inverse  
 method to detect small wavelength changes in basal slip which are physically  
 realistic for many ice flows.

## 6. Conclusion

Overall, the findings presented in this paper reinforce that it is possible  
 355 to recover both ice thickness and basal slip from surface data. The method  
 performed well in all test cases showing that it is robust regardless of underlying  
 bedrock or basal slip. Solutions were good for noisy measurements in the  
 accumulation function and surface speed. The relatively poor solution for noisy  
 surface elevation indicate that this measurement is one of the most important  
 360 for accuracy which can help to inform scientists in the field. This is a key result  
 when considering the applicability of the method to ‘real world’ problems in  
 which bedrock and basal slip are unlikely to be uniform or perfectly measured.

Many previous authors have focused on bedrock recovery in no-slip cases, or  
 have recovered bedrock with basal slip by having some prior measurements of  
 365 ice thickness. This method requires no such prior knowledge making it powerful  
 comparatively. Additionally, in studies where basal slip is included, methods to  
 date have been complex in comparison. The relatively simple method presented  
 here can accurately predict ice thickness and basal slip distribution for certain  
 broadly realistic synthetic cases.

## 370 Acknowledgements

This work was supported by the University of Canterbury Doctoral Scholarship and the Edward and Isabel Kidson Scholarship.

## References

- [1] Mathieu Morlighem et al. “Deep glacial troughs and stabilizing ridges unveiled beneath the margins of the Antarctic ice sheet”. In: *Nature Geoscience* 13.2 (Feb. 2020), pp. 132–137. ISSN: 17520908. DOI: [10.1038/s41561-019-0510-8](https://doi.org/10.1038/s41561-019-0510-8). 375
- [2] M. J. Raymond and G. H. Gudmundsson. “Estimating basal properties of ice streams from surface measurements: a non-linear Bayesian inverse approach applied to synthetic data”. In: *The Cryosphere* 3.2 (Dec. 2009), pp. 265–278. ISSN: 1994-0424. DOI: [10.5194/tc-3-265-2009](https://doi.org/10.5194/tc-3-265-2009). 380
- [3] Olalekan Babaniyi et al. “Inferring the basal sliding coefficient field for the Stokes ice sheet model under rheological uncertainty”. In: *Cryosphere* 15.4 (Apr. 2021), pp. 1731–1750. ISSN: 19940424. DOI: [10.5194/tc-15-1731-2021](https://doi.org/10.5194/tc-15-1731-2021). 385
- [4] “Summary for Policymakers”. In: *IPCC Special Report on the Ocean and Cryosphere in a Changing Climate*. Ed. by H.-O. Portner et al. 2019.
- [5] NOAA. *What is the Cryosphere?* 2019.
- [6] J. A. Church et al. “Sea Level Change”. In: *Climate Change 2013: The Physical Science Basis. Contribution of Working Group I to the Fifth Assessment Report of the Intergovernmental Panel on Climate Change*. Ed. by T. F. Stocker et al. Cambridge University Press, Cambridge, United Kingdom and New York, NY, USA., 2013. Chap. 13, pp. 1137–1216. 390
- [7] Ralf Greve and Heinz Blatter. *Dynamics of Ice Sheets and Glaciers*. Advances in Geophysical and Environmental Mechanics and Mathematics. Berlin, Heidelberg: Springer Berlin Heidelberg, 2009. ISBN: 978-3-642-03414-5. DOI: [10.1007/978-3-642-03415-2](https://doi.org/10.1007/978-3-642-03415-2). 395

- [8] Kolumban Hutter. “The Effect of Longitudinal Strain on the Shear Stress of an Ice Sheet: In Defence of Using Stretched Coordinates”. In: *Journal of Glaciology* 27.95 (Jan. 1981), pp. 39–56. ISSN: 0022-1430. DOI: [10.3189/S0022143000011217](https://doi.org/10.3189/S0022143000011217).
- [9] A. C. Fowler. “Sliding with Cavity Formation”. In: *Journal of Glaciology* 33.115 (Jan. 1987), pp. 255–267. ISSN: 0022-1430. DOI: [10.3189/S0022143000008820](https://doi.org/10.3189/S0022143000008820).
- [10] Heinz Blatter, Ralf Greve, and Ayako Abe-Ouchi. “Present State and Prospects of Ice Sheet and Glacier Modelling”. In: *Surveys in Geophysics* 32.4-5 (Sept. 2011), pp. 555–583. ISSN: 0169-3298. DOI: [10.1007/s10712-011-9128-0](https://doi.org/10.1007/s10712-011-9128-0).
- [11] Surendra Adhikari and Shawn J. Marshall. “Parameterization of lateral drag in flowline models of glacier dynamics”. In: *Journal of Glaciology* 58.212 (2012), pp. 1119–1132. ISSN: 0022-1430. DOI: [DOI:10.3189/2012JoG12J018](https://doi.org/10.3189/2012JoG12J018).
- [12] Daniel Farinotti et al. “How accurate are estimates of glacier ice thickness? Results from ITMIX, the Ice Thickness Models Intercomparison eXperiment”. In: *The Cryosphere* 11.2 (Apr. 2017), pp. 949–970. ISSN: 1994-0424. DOI: [10.5194/tc-11-949-2017](https://doi.org/10.5194/tc-11-949-2017).
- [13] Victor Barcilon and Douglas R. MacAyeal. “Steady flow of a viscous ice stream across a no-slip/free-slip transition at the bed”. In: *Journal of Glaciology* 39.131 (Jan. 1993), pp. 167–185. ISSN: 0022-1430. DOI: [10.3189/S0022143000015811](https://doi.org/10.3189/S0022143000015811).
- [14] A.V. Wilchinsky and V.A. Chugunov. “Modelling ice flow in various Glacier zones”. In: *Journal of Applied Mathematics and Mechanics* 65.3 (Jan. 2001), pp. 479–493. ISSN: 0021-8928. DOI: [10.1016/S0021-8928\(01\)00054-5](https://doi.org/10.1016/S0021-8928(01)00054-5).
- [15] Surendra Adhikari and Shawn J Marshall. “Improvements to shear-deformational models of glacier dynamics through a longitudinal stress factor”. In: *Journal of Glaciology* 57.206 (2011).

- [16] A. Gessese et al. “Direct reconstruction of glacier bedrock from known free surface data using the one-dimensional shallow ice approximation”. In: *Geomorphology* 228 (Jan. 2015), pp. 356–371. ISSN: 0169-555X. DOI: [10.1016/J.GEOMORPH.2014.09.015](https://doi.org/10.1016/J.GEOMORPH.2014.09.015).  
430
- [17] C Heining and M Sellier. “Direct Reconstruction of Three-dimensional Glacier Bedrock and Surface Elevation from Free Surface Velocity”. In: *AIMS Geosciences* 2.1 (2016), pp. 45–63. DOI: [10.3934/geosciences.2016.1.63](https://doi.org/10.3934/geosciences.2016.1.63).
- 435 [18] Hester Jiskoot. “Dynamics of Glaciers”. In: *Encyclopedia of Snow, Ice and Glaciers*. Ed. by Vijay P Singh, Pratap Singh, and Umesh K Haritashya. Dordrecht: Springer Netherlands, 2011, pp. 245–256. ISBN: 978-90-481-2642-2.
- [19] Kurt M. Cuffey and W. S. B. Paterson. *The Physics of Glaciers*. Elsevier Science & Technology Books, 2010. ISBN: 9780080919126.  
440
- [20] N. Martin and J. Monnier. “Inverse rheometry and basal properties inference for pseudoplastic geophysical flows”. In: *European Journal of Mechanics - B/Fluids* 50 (Mar. 2015), pp. 110–126. ISSN: 09977546. DOI: [10.1016/j.euromechflu.2014.11.011](https://doi.org/10.1016/j.euromechflu.2014.11.011).
- 445 [21] Jerome Monnier and Pierre-Emmanuel E. des Bosc. “Inference of the Bottom Properties in Shallow Ice Approximation Models”. In: *Inverse Problems* 33.11 (June 2017). ISSN: 13616420. DOI: [10.1088/1361-6420/aa7b92](https://doi.org/10.1088/1361-6420/aa7b92).
- [22] Ed Bueler and Jed Brown. “Shallow shelf approximation as a “sliding law” in a thermomechanically coupled ice sheet model”. In: *Journal of Geophysical Research* 114.F3 (July 2009), F03008. ISSN: 0148-0227. DOI: [10.1029/2008JF001179](https://doi.org/10.1029/2008JF001179).  
450
- [23] L W Morland. “Unconfined Ice-Shelf Flow”. In: Jan. 1987, pp. 99–116. DOI: [10.1007/978-94-009-3745-1\\_6](https://doi.org/10.1007/978-94-009-3745-1_6).

- 455 [24] D. R. Macayeal. “Large-scale ice flow over a viscous basal sediment: theory and application to ice stream B, Antarctica”. In: *Journal of Geophysical Research* 94.134 (Apr. 1989), pp. 4071–4087. ISSN: 01480227. DOI: [10.1029/jb094ib04p04071](https://doi.org/10.1029/jb094ib04p04071).
- [25] Valentina Zorzut et al. “Slope estimation influences on ice thickness inversion models: A case study for Monte Tronador glaciers, North Patagonian Andes”. In: *Journal of Glaciology* 66.260 (Dec. 2020), pp. 996–1005. ISSN: 00221430. DOI: [10.1017/jog.2020.64](https://doi.org/10.1017/jog.2020.64).
- 460 [26] Jérôme Monnier and Jiamin Zhu. “Inference of the bottom topography in anisothermal mildly-sheared shallow ice flows”. In: *Computer Methods in Applied Mechanics and Engineering* 348 (May 2019), pp. 954–977. ISSN: 0045-7825. DOI: [10.1016/J.CMA.2019.01.003](https://doi.org/10.1016/J.CMA.2019.01.003).
- [27] Teresa M. Kyrke-Smith, G. Hilmar Gudmundsson, and Patrick E. Farrell. “Can Seismic Observations of Bed Conditions on Ice Streams Help Constrain Parameters in Ice Flow Models?” In: *Journal of Geophysical Research: Earth Surface* 122.11 (Nov. 2017), pp. 2269–2282. ISSN: 21699003. DOI: [10.1002/2017JF004373](https://doi.org/10.1002/2017JF004373).
- 470 [28] Teresa M. Kyrke-Smith, G. Hilmar Gudmundsson, and Patrick E. Farrell. “Relevance of detail in basal topography for basal slipperiness inversions: A case study on Pine Island Glacier, Antarctica”. In: *Frontiers in Earth Science* 6 (Apr. 2018). ISSN: 22966463. DOI: [10.3389/feart.2018.00033](https://doi.org/10.3389/feart.2018.00033).
- 475 [29] Gong Cheng and Per Lötstedt. “Parameter sensitivity analysis of dynamic ice sheet models - Numerical computations”. In: *Cryosphere* 14.2 (Feb. 2020), pp. 673–691. ISSN: 19940424. DOI: [10.5194/tc-14-673-2020](https://doi.org/10.5194/tc-14-673-2020). arXiv: [1906.08209](https://arxiv.org/abs/1906.08209).
- 480 [30] J. W. Glen. “Experiments on the Deformation of Ice”. In: *Journal of Glaciology* 2.12 (Jan. 1952), pp. 111–114. ISSN: 0022-1430. DOI: [10.3189/S0022143000034067](https://doi.org/10.3189/S0022143000034067).

- [31] J.F. Nye. “The flow law of ice from measurements in glacier tunnels, laboratory experiments and the Jungfraufirn borehole experiment”. In: *Proceedings of the Royal Society of London. Series A. Mathematical and Physical Sciences* 219.1139 (Oct. 1953), pp. 477–489. DOI: [10.1098/rspa.1953.0161](https://doi.org/10.1098/rspa.1953.0161).
- [32] J. Weertman. “On the Sliding of Glaciers”. In: *Journal of Glaciology* 3.21 (Jan. 1957), pp. 33–38. ISSN: 0022-1430. DOI: [10.3189/S0022143000024709](https://doi.org/10.3189/S0022143000024709).
- [33] L. Lliboutry. “General Theory of Subglacial Cavitation and Sliding of Temperate Glaciers”. In: *Journal of Glaciology* 7.49 (Jan. 1968), pp. 21–58. ISSN: 0022-1430. DOI: [10.3189/S0022143000020396](https://doi.org/10.3189/S0022143000020396).
- [34] W. F. Budd, P. L. Keage, and N. A. Blundy. “Empirical Studies of Ice Sliding”. In: *Journal of Glaciology* 23.89 (Jan. 1979), pp. 157–170. ISSN: 0022-1430. DOI: [10.3189/S0022143000029804](https://doi.org/10.3189/S0022143000029804).
- [35] Hans Petter Langtangen and Anders Logg. *Solving PDEs in Python*. Springer International Publishing, 2016. DOI: [10.1007/978-3-319-52462-7](https://doi.org/10.1007/978-3-319-52462-7).
- [36] Anders Logg, Kent-Andre Mardal, Garth N Wells, et al. *Automated Solution of Differential Equations by the Finite Element Method*. Springer, 2012. ISBN: 978-3-642-23098-1. DOI: [10.1007/978-3-642-23099-8](https://doi.org/10.1007/978-3-642-23099-8).
- [37] Martin S Alnæs, Anders Logg, and Kent-Andre Mardal. “UFC: a Finite Element Code Generation Interface”. In: *Automated Solution of Differential Equations by the Finite Element Method, Volume 84 of Lecture Notes in Computational Science and Engineering*. Ed. by Anders Logg, Kent-Andre Mardal, and Garth N Wells. Springer, 2012. Chap. 16.
- [38] Satish Balay et al. *{PETS}c {W}eb page*. [url{https://www.mcs.anl.gov/petsc}](https://www.mcs.anl.gov/petsc). 2021.
- [39] Satish Balay et al. *{PETS}c Users Manual*. Tech. rep. ANL-95/11 - Revision 3.15. Argonne National Laboratory, 2021.

- [40] Satish Balay et al. “Efficient Management of Parallelism in Object Oriented Numerical Software Libraries”. In: *Modern Software Tools in Scientific Computing*. Ed. by E Arge, A M Bruaset, and H P Langtangen. Birkhäuser Press, 1997, pp. 163–202.
- 515 [41] Emmanuel Le Meur et al. “Glacier flow modelling: a comparison of the Shallow Ice Approximation and the full-Stokes solution”. In: *Comptes Rendus Physique* 5.7 (Sept. 2004), pp. 709–722. ISSN: 1631-0705. DOI: [10.1016/J.CRHY.2004.10.001](https://doi.org/10.1016/J.CRHY.2004.10.001).
- [42] A. Gessesse. “Algorithms for bed topography reconstruction in geophysical flows”. PhD thesis. University of Canterbury, 2014.
- 520 [43] Elizabeth K. McGeorge et al. “Bedrock reconstruction from free surface data for unidirectional glacier flow with basal slip”. In: *Acta Mechanica* 232.1 (Jan. 2021), pp. 305–322. ISSN: 16196937. DOI: [10.1007/s00707-020-02845-x](https://doi.org/10.1007/s00707-020-02845-x). arXiv: [2006.13310](https://arxiv.org/abs/2006.13310).
- 525 [44] Yee Lo Keung and Jun. Zou. “An efficient linear solver for nonlinear parameter identification problems”. In: *SIAM Journal on Scientific Computing* 22.5 (2000), pp. 1511–1526. ISSN: 10648275. DOI: [10.1137/S1064827598346740](https://doi.org/10.1137/S1064827598346740).
- [45] Zhiming Chen and Jun Zou. “An augmented lagrangian method for identifying discontinuous parameters in elliptic systems”. In: *SIAM Journal on Control and Optimization* 37.3 (1999), pp. 892–910. ISSN: 03630129. DOI: [10.1137/S0363012997318602](https://doi.org/10.1137/S0363012997318602).
- 530 [46] Damián Fernández and Mikhail Solodov. “On the cost of solving augmented Lagrangian subproblems”. In: *Mathematical Programming* 182.1-2 (July 2020), pp. 37–55. ISSN: 14364646. DOI: [10.1007/s10107-019-01384-1](https://doi.org/10.1007/s10107-019-01384-1).
- 535 [47] G. H. Gudmundsson and M. Raymond. “On the limit to resolution and information on basal properties obtainable from surface data on ice streams”. In: *The Cryosphere* 2.2 (Dec. 2008), pp. 167–178. ISSN: 1994-0424. DOI: [10.5194/tc-2-167-2008](https://doi.org/10.5194/tc-2-167-2008).